

ANALYSIS OF TETHERED BALLOON DATA FROM SAN NICOLAS ISLAND ON 8 JULY 1987

STEPHEN K. COX

DAVID P. DUDA

THOMAS A. GUINN

CHRISTOPHER M. JOHNSON-PASQUA

WAYNE H. SCHUBERT

Department of Atmospheric Science, Colorado State University, Fort Collins, Colorado 80523

JACK B. SNIDER

NOAA/ERL/Wave Propagation Laboratory, Boulder, Colorado 80503

(June 1988)

1. Introduction

This paper summarizes our analysis of the 8 July 1987 (Julian Day 189) tethered balloon flight from San Nicolas Island. The flight commenced at about 14:30 UTC (7:30 Pacific Daylight Time) and lasted six and one-half hours. The position of the CSU instrument package as a function of time is shown in Fig. 1. For the purpose of presentation of results we have divided the flight into the 13 legs indicated in Fig. 1. These legs consist of 20 minute constant level runs, with the exception of leg 1, which is a sounding from the surface to just above 930 mb. The laser ceilometer (Schubert et al., 1987) record of cloud base is also shown in Fig. 1. The cloud base averaged around 970 mb during much of the flight but was more variable near the end.

Before the tethered balloon flight commenced, a CLASS sounding (Schubert et al., 1987) was released at 12:11 UTC (5:11 PDT). Temperature and moisture data below 927 mb for this sounding is shown in Figure 2. The sounding indicates a cloud top around 955 mb at this time.

2. Some Basic Theory

In order to interpret the tethered balloon data, some basic theory is required. Define the saturation moist static energy as $h^* = c_p T + gz + Lq^*$, where q^* is the saturation mixing ratio. The moist adiabatic lapse rate is derived by

setting $\partial h^* / \partial z = 0$, which leads directly to

$$\frac{\partial T}{\partial z} + \frac{g}{c_p} = -\frac{L}{c_p} \frac{\partial q^*}{\partial z}. \quad (2.1)$$

Since q^* is a function of T and p , we have

$$\frac{\partial q^*}{\partial z} = \left(\frac{\partial q^*}{\partial T} \right)_p \frac{\partial T}{\partial z} + \left(\frac{\partial q^*}{\partial p} \right)_T \frac{\partial p}{\partial z}. \quad (2.2)$$

Using the hydrostatic approximation, this can be written

$$\frac{L}{c_p} \frac{\partial q^*}{\partial z} = \gamma \frac{\partial T}{\partial z} + \frac{g}{R} \frac{Lq^*}{c_p T}, \quad (2.3)$$

where

$$\gamma = \frac{L}{c_p} \left(\frac{\partial q^*}{\partial T} \right)_p. \quad (2.4)$$

Eliminating $\frac{\partial q^*}{\partial z}$ between (2.1) and (2.3) we obtain the moist adiabatic lapse rate

$$-\frac{\partial T}{\partial z} = \frac{g}{c_p} \left(\frac{1 + \frac{Lq^*}{RT}}{1 + \gamma} \right). \quad (2.5)$$

Since the dry adiabatic lapse rate is g/c_p , the last factor in (2.5) gives the ratio of the moist and dry adiabatic lapse rates. Using $g = 9.80 \text{ m s}^{-2}$, $c_p = 1004.5 \text{ J kg}^{-1} \text{ K}^{-1}$, $L = 2.47 \times 10^6$

$J \text{ kg}^{-1}$, $R = 287 \text{ J kg}^{-1} \text{ K}^{-1}$, $q^* = 9.5 \text{ g kg}^{-1}$, $T = 285.65 \text{ K}$ and $\gamma = 1.34$, we obtain

$$-\frac{\partial T}{\partial z} = \begin{cases} 0.00536 \text{ K m}^{-1} & \text{in cloud layer,} \\ 0.00976 \text{ K m}^{-1} & \text{in subcloud layer,} \end{cases} \quad (2.6)$$

or

$$\frac{\partial T}{\partial p} = \begin{cases} 0.0448 \text{ K mb}^{-1} & \text{in cloud layer,} \\ 0.0816 \text{ K mb}^{-1} & \text{in subcloud layer.} \end{cases} \quad (2.7)$$

Eliminating $\partial T/\partial z$ between (2.1) and (2.3), and assuming that the total water $q^* + \ell$ is mixed in the cloud layer we obtain

$$\frac{\partial \ell}{\partial z} = -\frac{\partial q^*}{\partial z} = \frac{g}{L} \left(\frac{\gamma - \frac{Lq^*}{RT}}{1 + \gamma} \right) \approx 0.00179 \text{ g kg}^{-1} \text{ m}^{-1} \quad (2.8)$$

If the liquid water mixing ratio ℓ is a linear function of height in the cloud layer, then

$$\int_{z_C}^{z_B} \ell \rho dz = \frac{\partial \ell}{\partial z} \frac{\rho}{2} (z_B - z_C)^2, \quad (2.9)$$

where $(z_B - z_C)$ is the depth of the cloud. Solving for $(z_B - z_C)$ we obtain

$$z_B - z_C = \left(\frac{\int \ell \rho dz}{\frac{\partial \ell}{\partial z} \frac{\rho}{2}} \right)^{\frac{1}{2}}. \quad (2.10)$$

3. Thermodynamic Data

Figure 3 shows profiles of dry bulb and wet bulb temperatures taken on leg 1 of Figure 1. Note that the brief constant level section of leg 1 at 935 mb was partially in and partially out of cloud; this leads to the large variance in temperature at 935 mb in Figure 3. The laser ceilometer reported a cloud base of 970 mb during the sounding, and this is indicated in Figure 3 by the kink between the dry and the moist adiabatic lapse rates. The fact that the wet bulb temperature increases with height just above cloud top indicates that the cloud layer is stable for evaporative instability processes. An interesting feature of Figure 3 is that the subcloud layer lapse rate is less than dry adiabatic, which is inconsistent with mixed layer theory; the value found from Figure 3 is about 7K/100m. If the boundary layer were warming at a rate of 1.8 K/hour, the time required for

the balloon to reach cloud base would explain the difference between the apparent lapse rate and the dry adiabatic lapse rate. Another (perhaps more likely) explanation is that there was evaporative cooling in the subcloud layer due to drizzle, which was quite noticeable at the surface at 17:30 UTC but was probably also present at earlier times.

A measurement of path-integrated liquid water (i.e. the numerator in (2.10)) was made by a microwave radiometer (Snider, 1988; Hogg et al., 1983). The data for 8 July is shown in Fig. 4. Using (2.8) and (2.10) the path integrated liquid water can be converted to cloud depth with 0.05, 0.10, 0.15, 0.20, 0.25 mm of liquid corresponding to cloud depths of 214, 303, 370, 428, 478 m respectively. Since the spike at 17:30 UTC in Fig. 4 would correspond to a cloud thickness of over 500 m, the transformation of path-integrated liquid water to cloud thickness is probably not valid at this particular time. Indeed, at 17:30 UTC drizzle was reported at the ground, which indicates there was probably considerable liquid in the subcloud layer.

4. Cloud Physics Data

a. instrumentation

Cloud droplet sizes and concentrations were measured with a PMS Forward Scattering Spectrometer Probe (FSSP) mounted on the front of the instrument platform. The FSSP operated in the diameter range between 2 and 47 μm . However, due to a problem in the data collection equipment, the values from two adjacent bins were stored in one bin, resulting in seven channels which are six microns in width and one channel 3 microns in width (44 - 47 μm). The values collected from the probe were from five second samples.

b. data reduction

From the raw FSSP data, liquid water content (LWC), mean droplet diameter (d_m) and number density (N) were calculated for each leg of the flight. The FSSP counts particles which sweep through a variable sampling area, which is based on the number of the total counts accepted by the velocity averaging circuitry in the instrument. The effective sampling area is

$$A_e = A \times AC \div TC,$$

where A is the measured sampling area ($2.8 \times 10^{-7} \text{ m}^2$), AC the total accepted counts, and TC the total counts (accepted + rejected). The sampling volume is

$$V = A_e v \delta t,$$

where v is the true airspeed and δt the sampling interval (5 seconds). Thus, the concentration of particles in one channel is

$$n_j = \frac{C_j}{V}$$

where C_j is the number of droplets counted in the j^{th} channel and the total number density is the summation of the particle concentrations in each channel,

$$N = \sum_{j=1}^{15} n_j.$$

The average droplet diameter in each of the channels is

$$d_j = \begin{cases} (6j - 1) & \text{for } 1 \leq j \leq 7 \\ 45.5 & \text{for } j = 8 \end{cases}$$

where d_j is expressed in microns. The mean diameter of the particles was computed from

$$d_m = \frac{1}{N} \sum_{j=1}^{15} n_j d_j$$

and the liquid water content was calculated from

$$LWC = \frac{\pi}{6} \rho_L \sum_{j=1}^{15} n_j d_j^3,$$

where ρ_L is the density of water.

c. results

Figures 5–7 present the liquid water content, the mean radius and the total number density respectively, which were measured during leg 5 of the balloon flight. This leg measured the microphysical properties near the top of the cloud at a level of 928.8 mb. At the start of the leg, it appears the instruments are above the cloud, but at 17:03 UTC the rapid increases in LWC and number density indicate the package has entered the cloud. The time series of the number density indicates the number density is 11 particles·cm⁻³ in this part of the cloud. The average concentration remains fairly constant during the leg, although there are large peaks at 17:13 UTC and 17:24 UTC which are over two times the average value. These peaks probably indicate problems with the data collection system.

The liquid water content near cloud top averages near 0.08 g·m⁻³, although there is some variability in the data. The measured liquid water content at this level is much lower than the values observed lower in the cloud, and it is suggested that the entrainment of the dry air above the cloud is producing the low LWC at this pressure. The points in the LWC curve follow the shape of the number density curve, and thus the sharp peaks result from the same problems which affect the number density data.

Figure 8 presents a profile of the liquid water content throughout the boundary layer. The points on the graph represent the average LWC in each of the twenty minute legs. The liquid water contents in the cloud were generally equal to the adiabatic LWC, with a peak value of 0.38 g·m⁻³ during leg 6 (947.7 mb). At the bottom of the cloud there is a peak of 0.30 g·m⁻³ but in the subcloud layer the LWC was near zero g·m⁻³. The number density and mean radius profiles are shown in Figure 9. The maximum concentrations occur in the top of the cloud, with values up to 130 particles·cm⁻³ during leg 6. As reflected in the LWC data, the number density in leg 9 is extremely high. The presence of such numerous particles is puzzling. It is not certain whether these particles are real or a problem with the FSSP counts.

Figure 10 shows a normalized droplet size distribution during leg 1 at 994.3 mb, which is in the subcloud layer. A majority (65%) of the particles are smaller than 8 μm in diameter, which suggests they may be haze particles. The small particles, however, appear to be dominant not only in the sub-cloud layer, but also inside and above the cloud.

5. Radiation Data

Figure 11 shows the net near infrared and longwave radiative fluxes measured during leg 1. Inside the cloud layer, from roughly 300 m to 600 m, the net longwave flux is nearly constant and approximately zero. At the top of the cloud layer there is strong longwave flux divergence, nearly -60 W m⁻². Inhomogeneties in the cloud structure produced variabilities in the net near IR flux inside the cloud. The variability is greatest near the top of the cloud deck, where the instrument platform passed through an uneven cloud top. Near the top of the cloud there is a convergence of shortwave radiation.

Table 1 presents radiation statistics for legs 2, 3 and 4 of the flight. Leg 2 (929 mb) and leg 3 (935 mb) were taken above cloud top. In both cases the net longwave flux is high and the standard deviation of measured downwelling short-

wave flux is low. Leg 4 (942 mb) was taken just below cloud top. At this height the standard deviation in downwelling shortwave flux is much higher than in the other legs and the net longwave flux is nearly zero. It should be noted that the total albedo above the cloud (at 929 mb) is 71.0 %, while the near IR albedo is 67.5 % and the visible albedo is 74.2 %.

Acknowledgments. Our participation in the FIRE project has been supported by the Marine Meteorology Program of the Office of Naval Research under contract N00014-87-K-0228 and by the National Aeronautics and Space Administration under contract NAG1-554.

REFERENCES

- Hogg, D.C., F.O. Guiraud, J.B. Snider, M.T. Decker, and E.R. Westwater, 1983: A steerable dual-channel microwave radiometer for measurement of water vapor and liquid in the troposphere. *J. Climate Appl. Meteorol.*, 22, 789-806.
- Particle Measuring Systems, Inc, 1984: Forward scattering spectrometer probe PMS model fssp-100, Operating and servicing manual, 58 pp.
- Schubert, W.H., P.E. Ciesielski, T.B. McKee, J.D. Kleist, S.K. Cox, C.M. Johnson-Pasqua, and W.L. Smith, Jr., 1987: Analysis of boundary layer sounding data from the FIRE marine stratocumulus project. *Atmos. Sci. Paper No. 419*, Dept. of Atmos. Sci., Colorado State University.
- Schubert, W.H., S.K. Cox, P.E. Ciesielski, and C.M. Johnson-Pasqua, 1987: Operation of a ceilometer during the FIRE marine stratocumulus experiment. *Atmos. Sci. Paper No. 420*, Dept. of Atmos. Sci., Colorado State University.
- Snider, J.B., 1988: Radiometric observations of cloud liquid water during FIRE. Preprint.

FIRE - SNI - FLT #3 - JD189 (8 JULY 87)

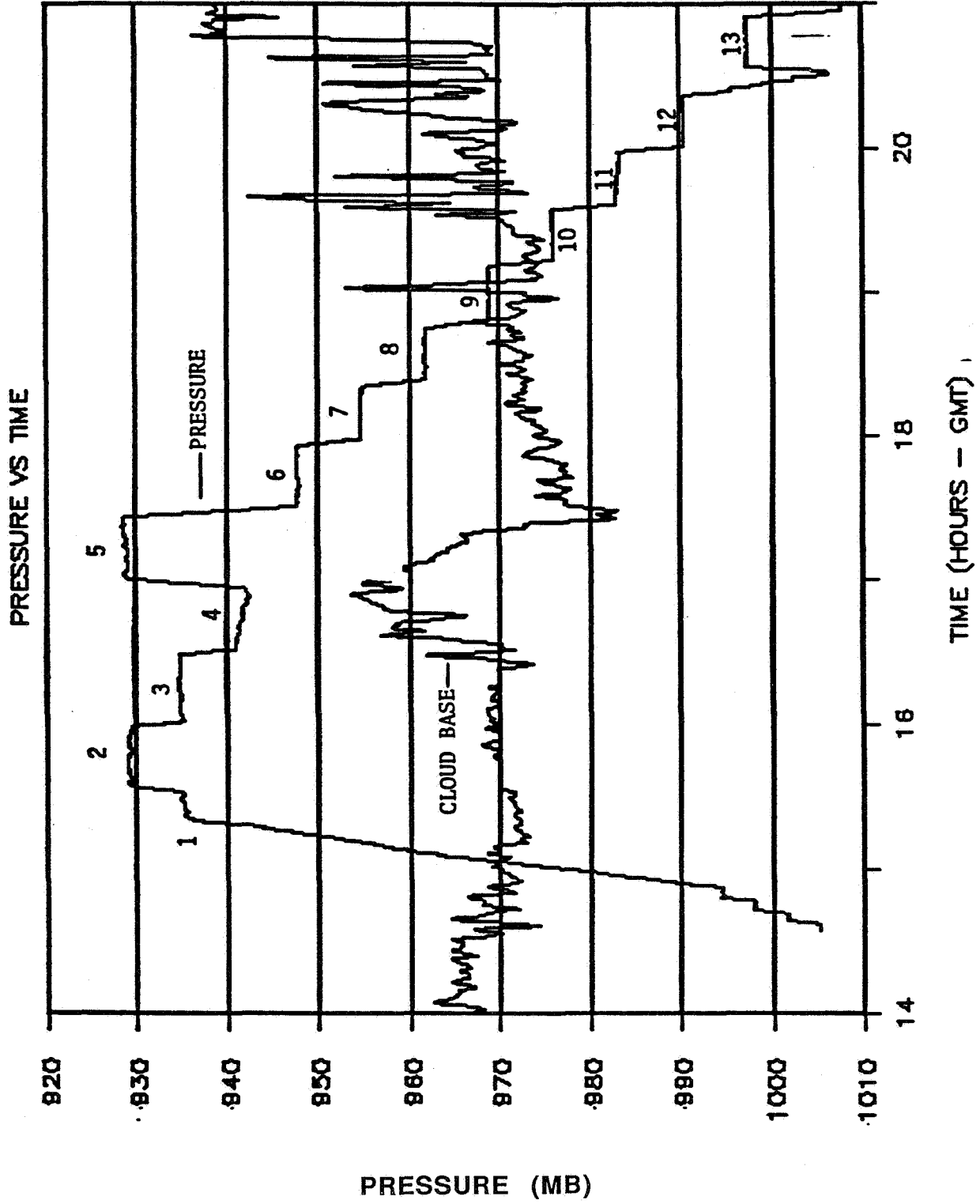


Figure 1

FIRE - SNI - JD189 1211Z (8 JULY 87)

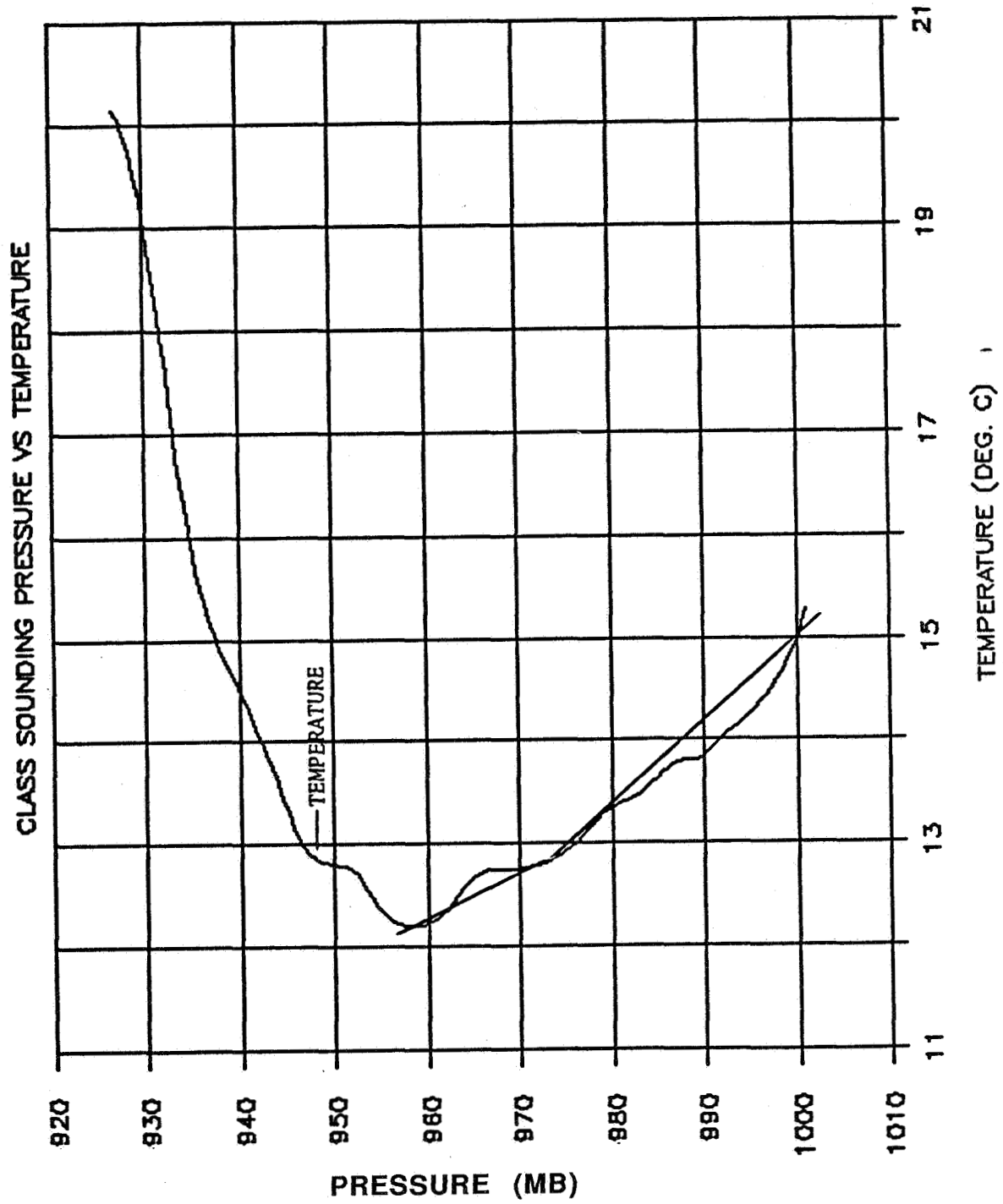


Figure 2a

FIRE - SNI - JD189 1211Z (8 JULY 87)

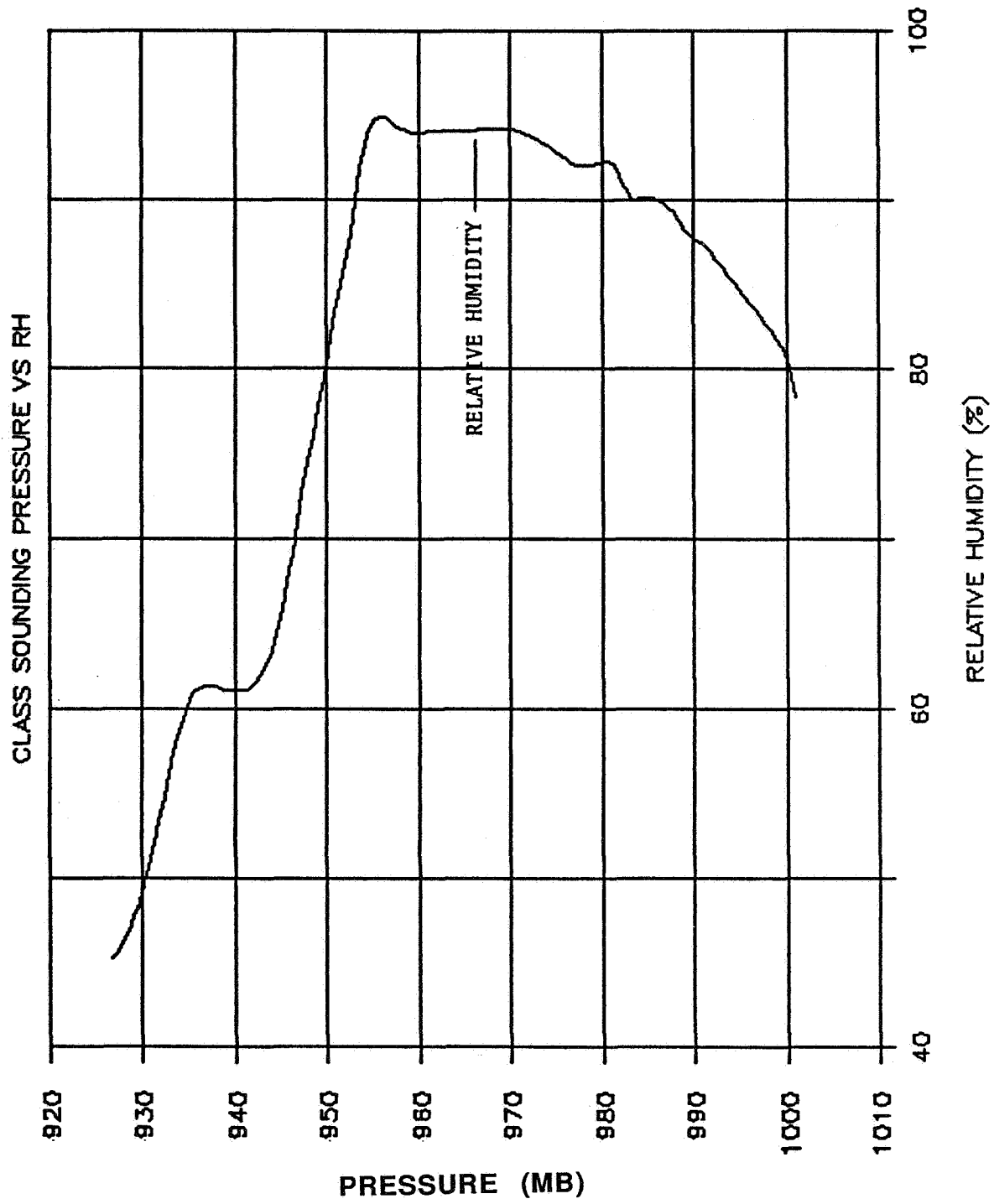


Figure 2b

FIRE - SNI - FLT #3 - JD189 (8 JULY 87)

LEG 1 WET AND DRY BULB TEMP. VS PRESS.

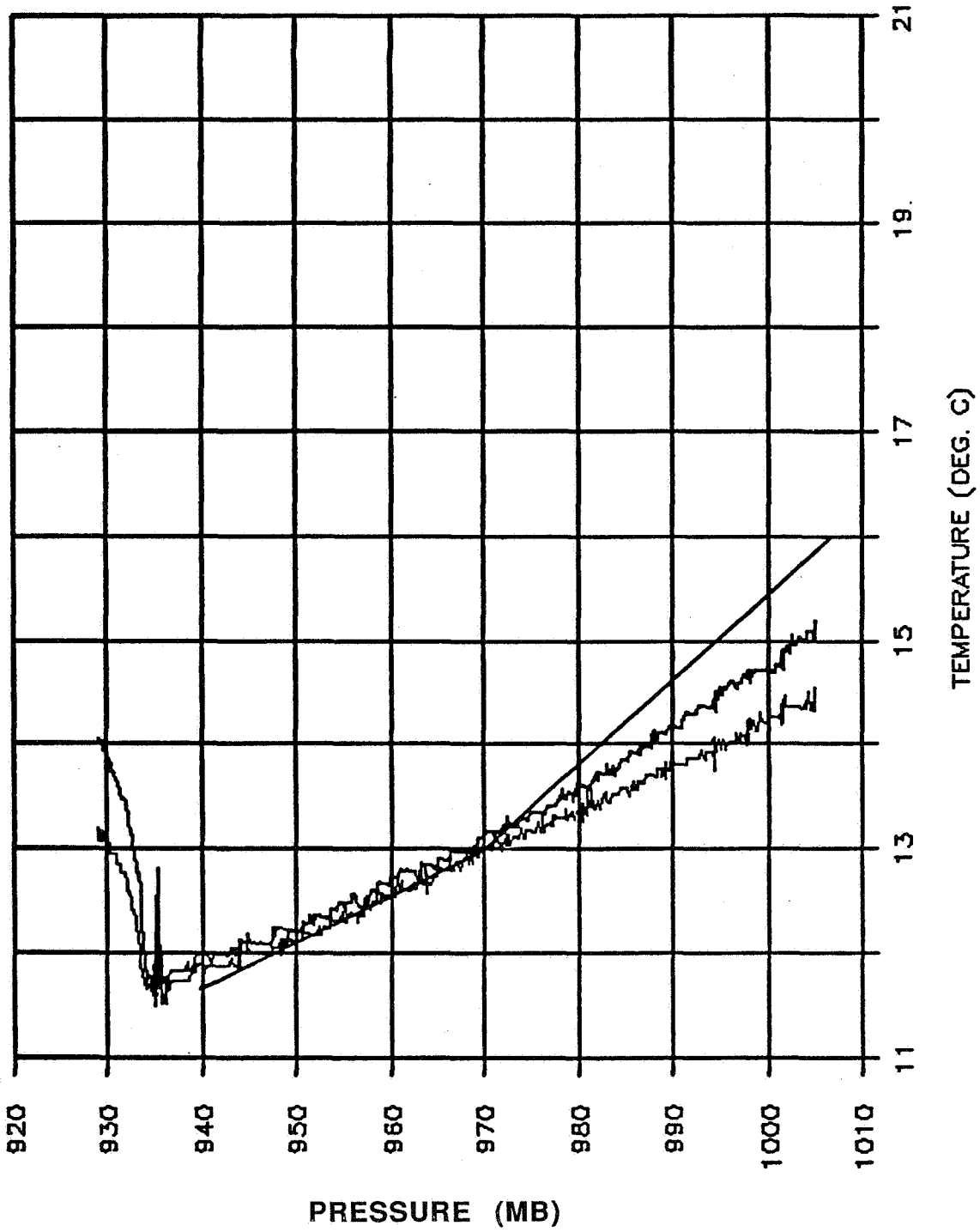


Figure 3

SAN NICOLAS ISLAND
STEERABLE RADIONETER DATA

DAY NO. 189
8 JUL 1987

AZIMUTH = 270.0 DEG
ELEVATION = 90.0 DEG

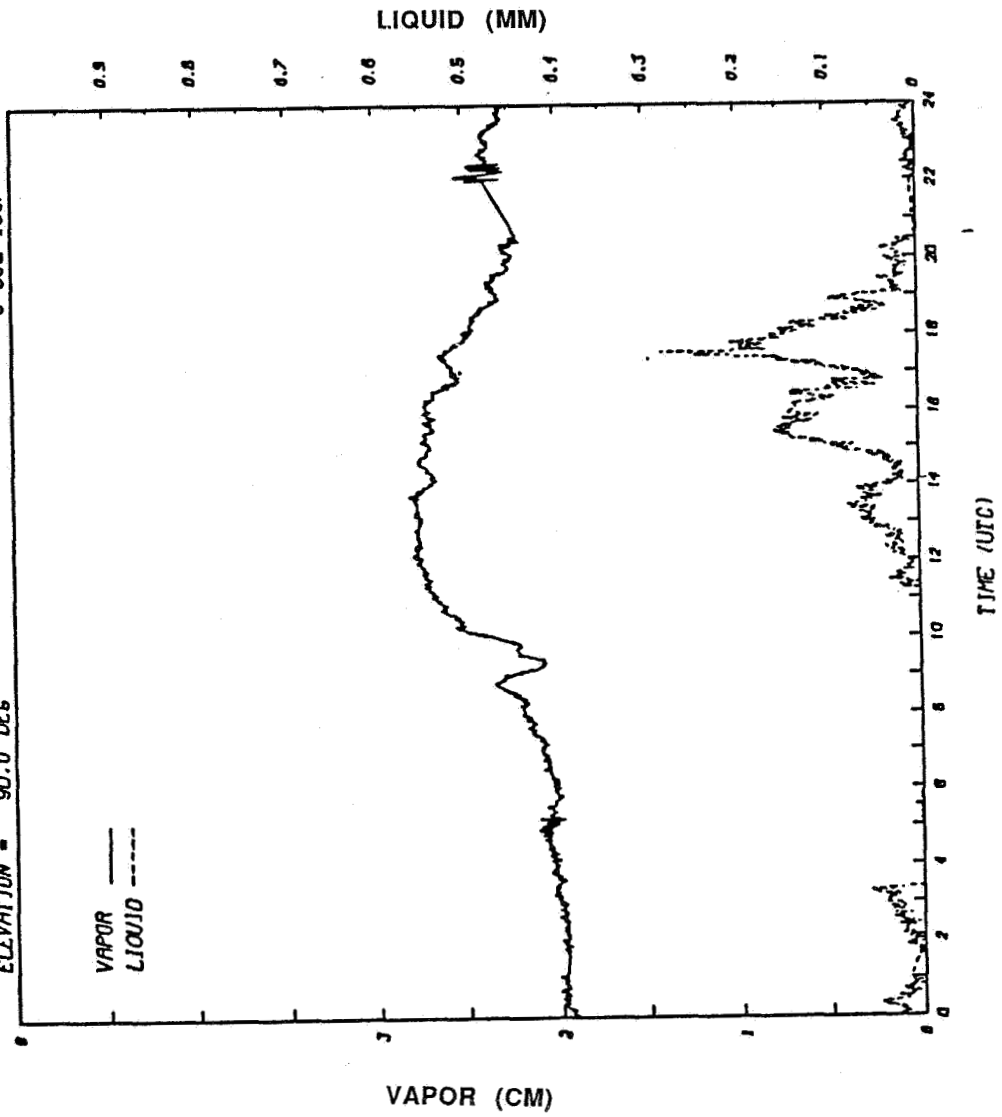


Figure 4

FIRE -- SNI FLT#3 -- JD189 (8 JULY 87)

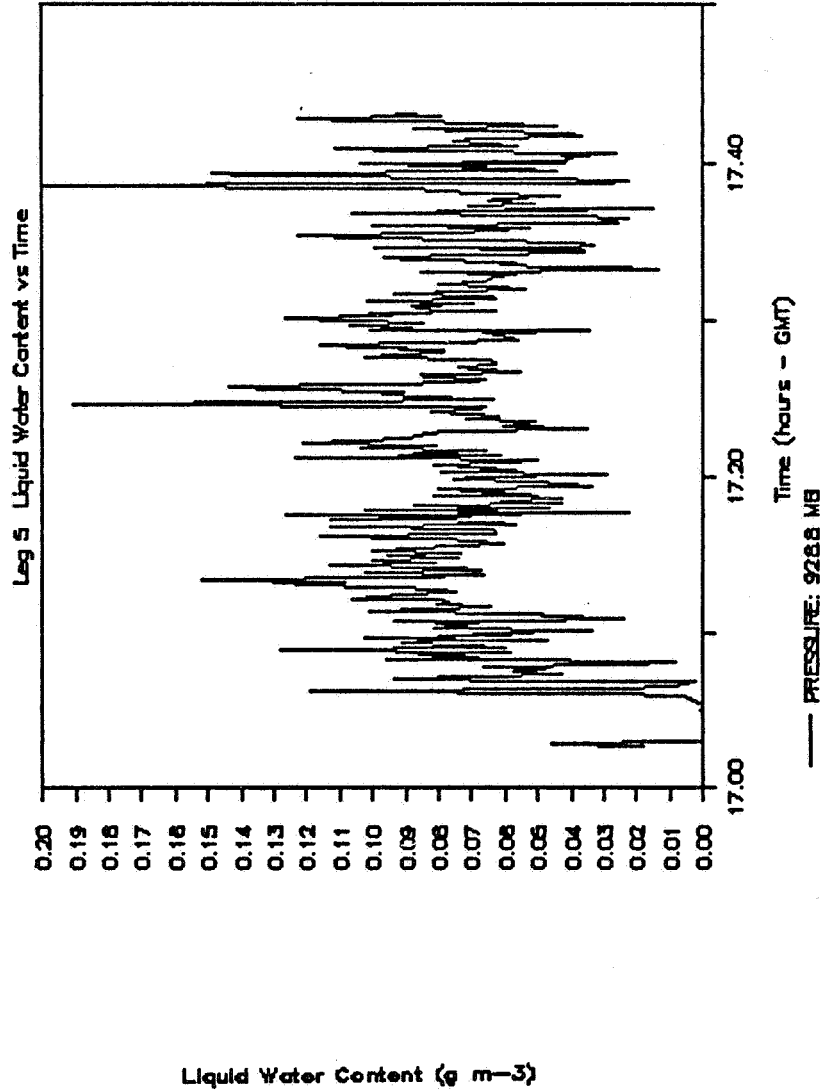


Figure 5

FIRE -- SNI FLT#3 -- JD 189 (8 JULY 87)

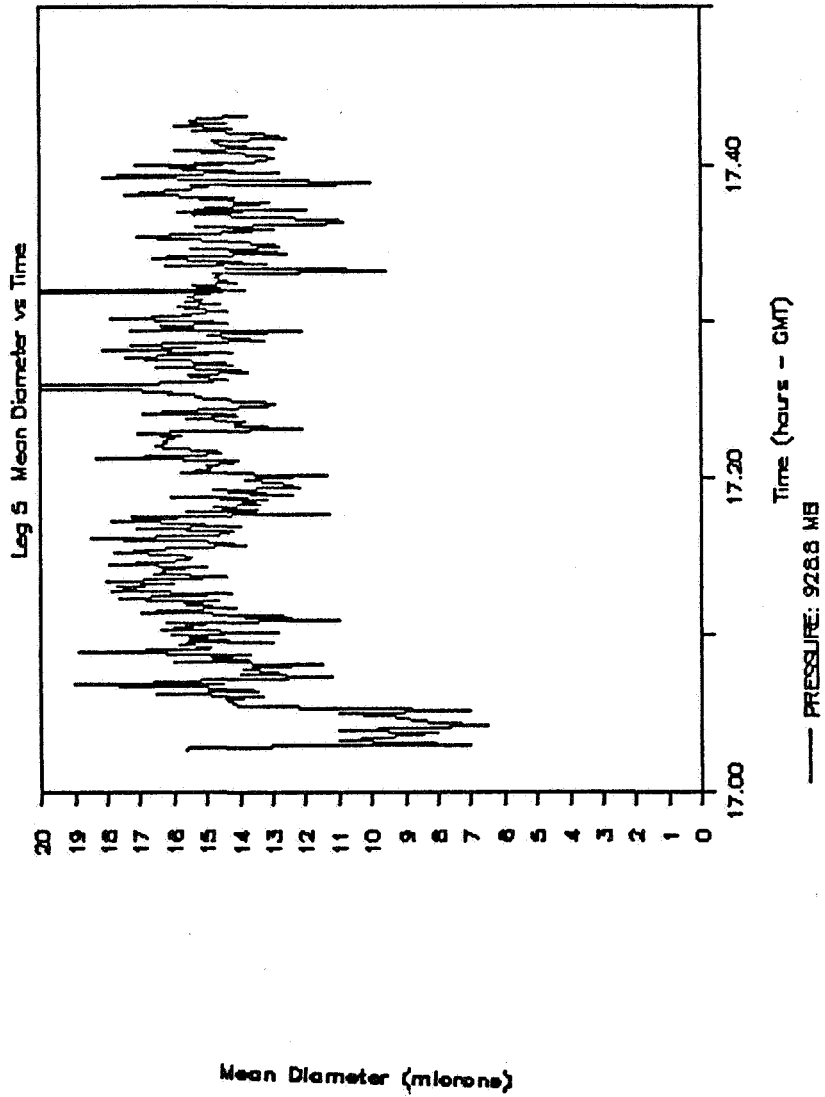


Figure 6

FIRE -- SNI FLT#3 -- JD189 (8 JULY 87)

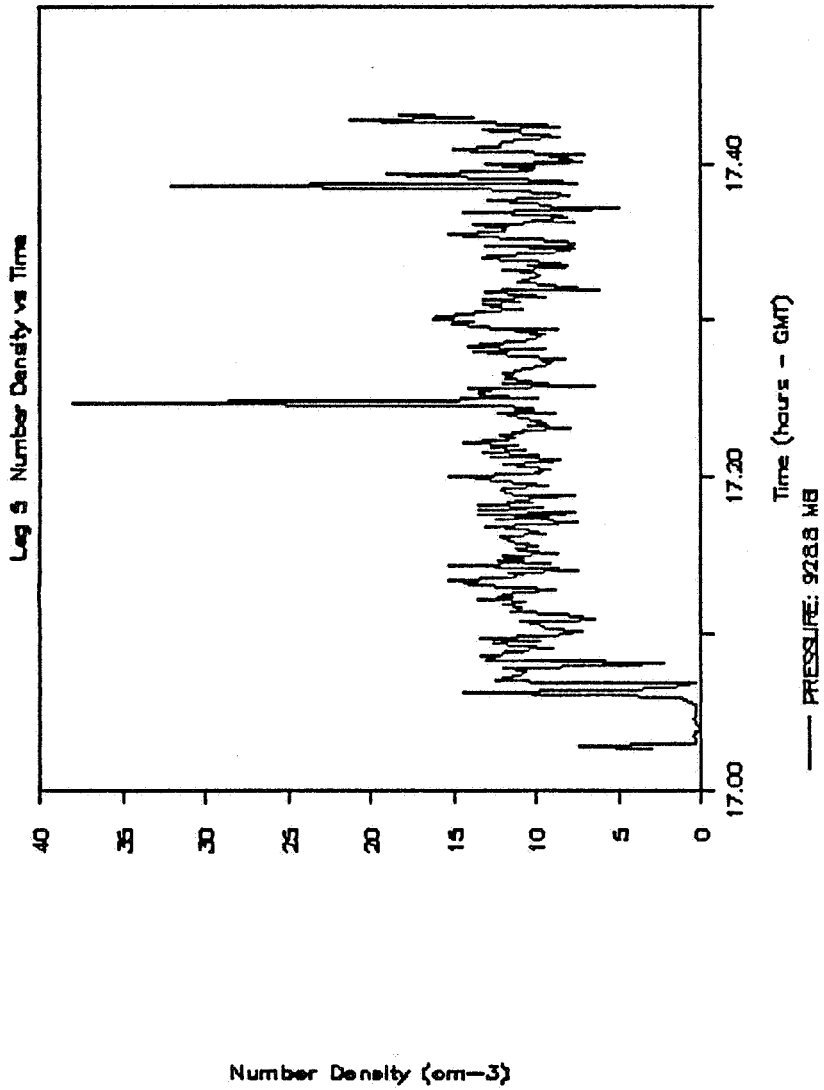


Figure 7

FIRE - SNI - FLT #3 - JD189 (8 JULY 87)

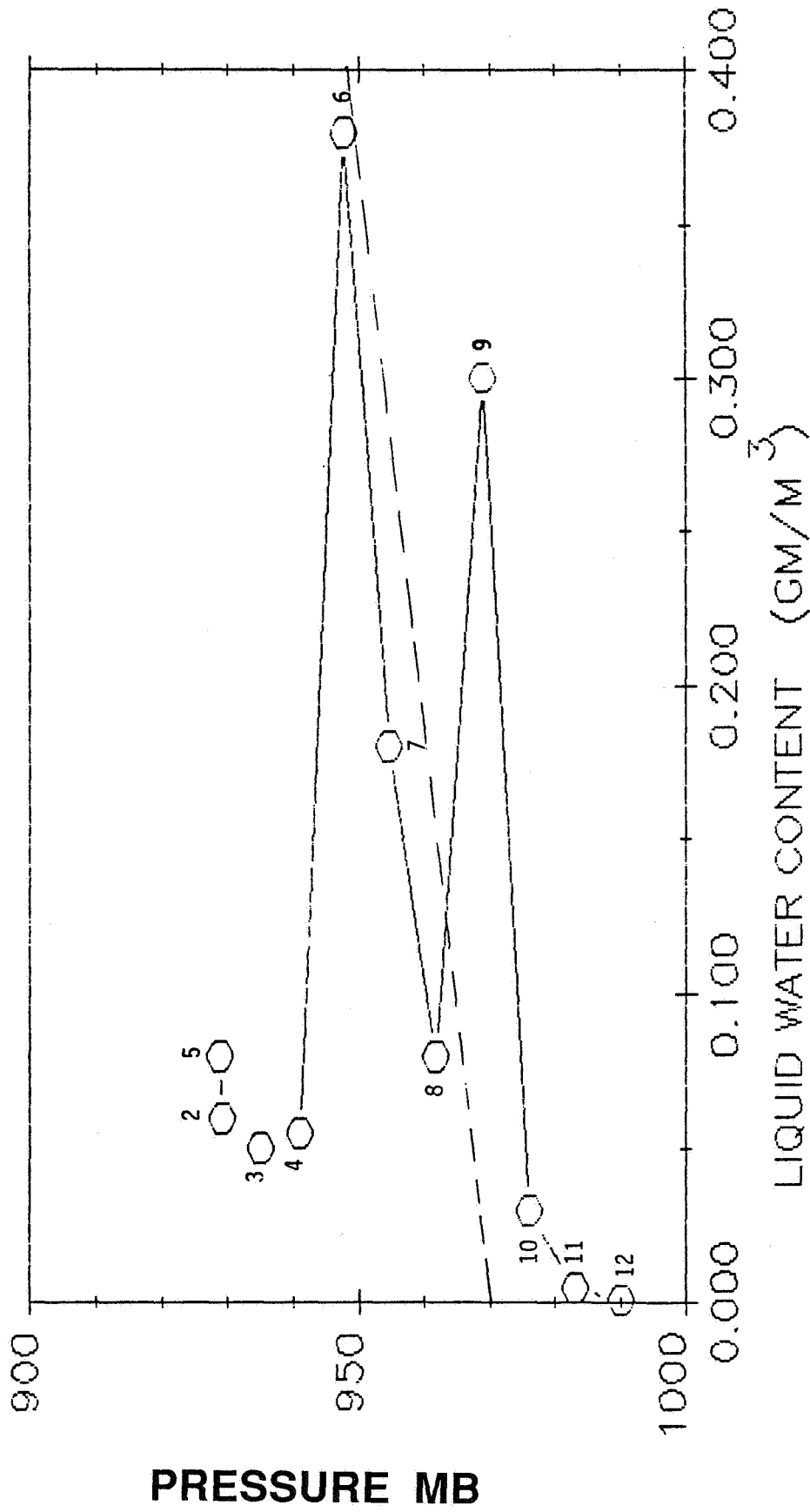


Figure 8

FIRE -- SNI -- FLT #3 -- JD189 (8 JULY 87)

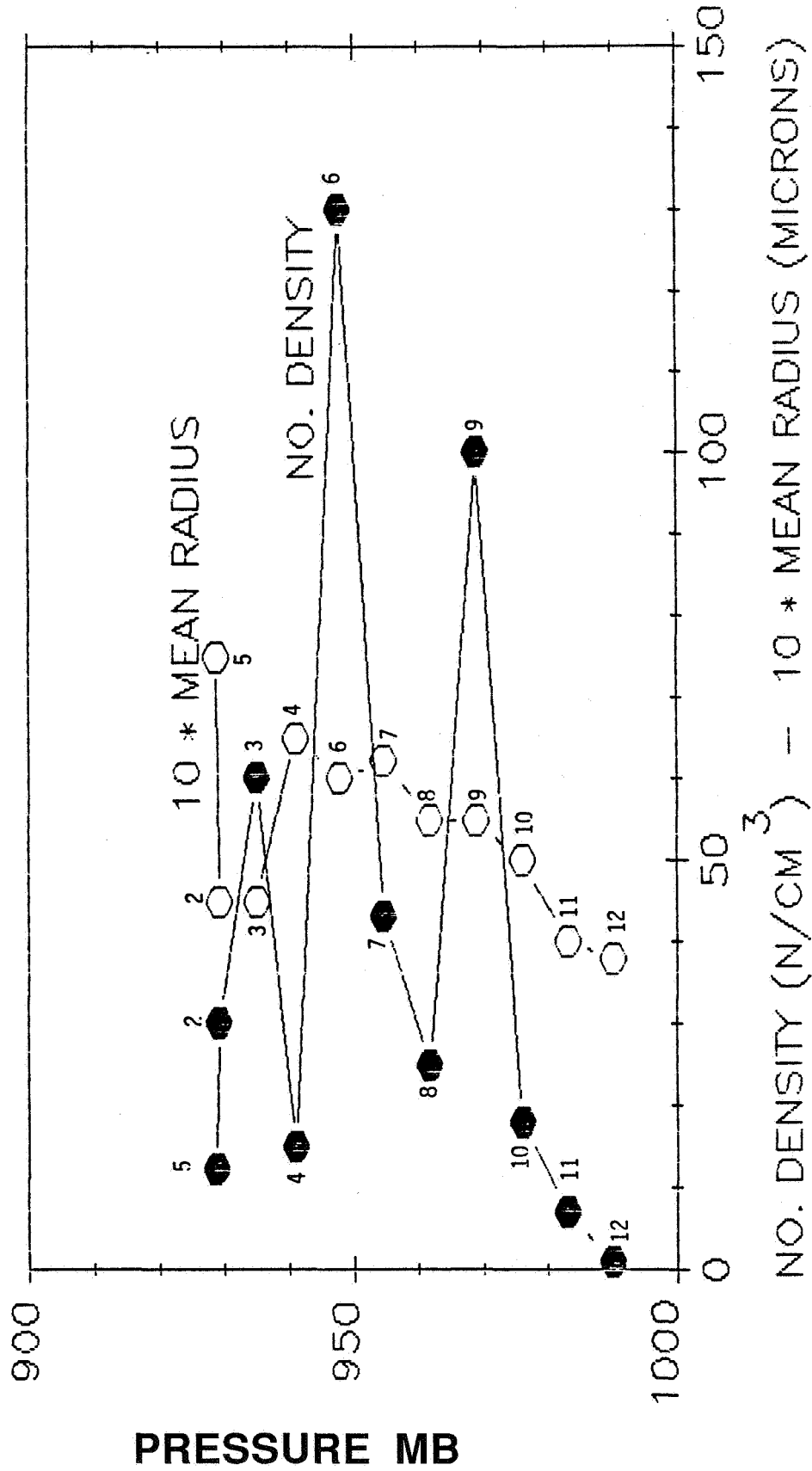


Figure 9

FIRE -- SNI FLT#3 -- JD189 (8 JULY 87)

Log 1 Normalized Drop Size Dist.

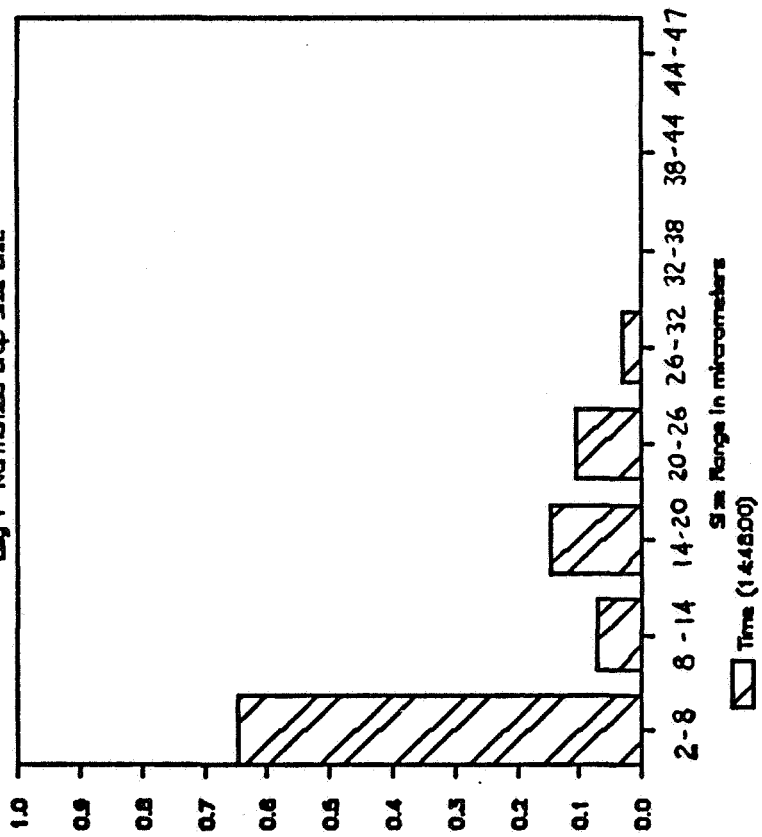


Figure 10

LEG 1 NET RADIATION PROFILE

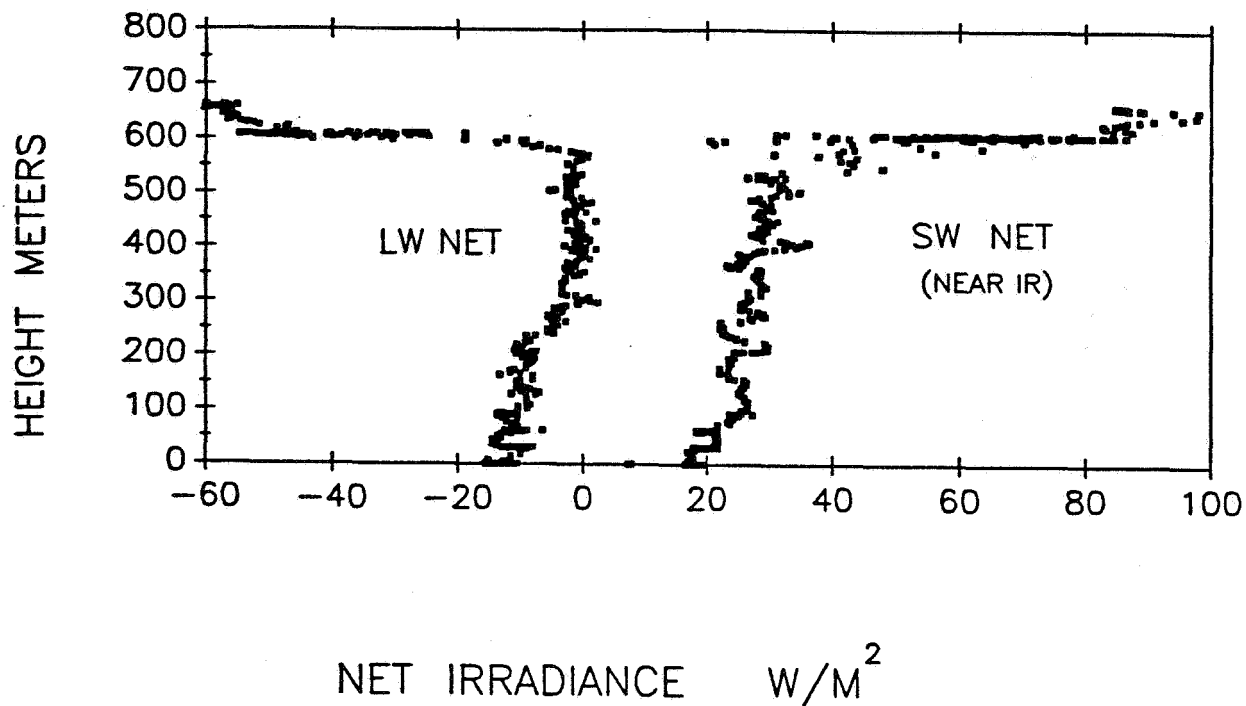


Figure 11

Table 1

RADIATION STATISTICS FOR DATA LEGS 2, 3 AND 4

Pres. mb		SW DN Wm^{-2}	SW UP Wm^{-2}	NIR DN Wm^{-2}	NIR UP Wm^{-2}	ALB TOT %	ALB NIR %	ALB VIS %	SW TOT NET Wm^{-2}	LW NET Wm^{-2}
929	Ave	616.0	437.0	296.2	199.8	71.0	67.5	74.2	179.0	-56.8
	SD	23.7	22.9	12.1	10.8	2.2	2.2	2.2	14.4	2.1
935	Ave	711.0	519.2	344.0	241.0	73.1	70.1	75.9	191.8	-53.5
	SD	30.0	25.1	15.0	12.4	2.7	2.6	2.8	23.4	5.1
942	Ave	618.0	364.0	294.7	173.1	59.4	59.3	59.6	253.9	0.1
	SD	85.8	57.0	42.5	27.0	9.2	8.8	9.5	78.0	4.3